

Investigation on Doppler Shift and Bandwidth of Backscattered Echoes From a Composite Sea Surface

Yunhua Wang and Yanmin Zhang

Abstract—In the general framework of the second-order small-slope approximation (SSA) (SSA-II), Doppler shifts of backscattered fields from time-varying sea surfaces are predicted at small and moderate incidence angles. The composite sea surface is modeled as a superposition of large-scale gravity waves and small-scale ripples. Here, the elevation of the large-scale surface component, on which each small facet travels along a closed orbit under the condition of the first-order approximation, is described by the coordinates of the small facets. The predicted Doppler shifts are compared with the results obtained by the small perturbation method (SPM), the geometrical optics method, the first-order SSA (SSA-I), and the two-scale scattering method (TSM). We can find that the predicted Doppler shifts for SPM and SSA-I in copolarized configuration are insensitive to the polarization state. However, the results obtained by SSA-II are consistent with those obtained by TSM and yield significant differences between HH and VV polarizations. Spectrum bandwidth is mainly induced by sea-surface orbit motions. In this paper, the formula of the spectrum bandwidth for the scattered echoes from the composite sea surface is also derived on the basis of TSM. The predicted bandwidths are compared with the Monte Carlo simulated results and the measured data. Furthermore, the dependences of the Doppler shift and the bandwidth on the parameters, such as the polarization, wind speed, radar frequency, etc., are also discussed.

Index Terms—Doppler shift, sea surface, spectrum bandwidth, second-order small-slope approximation (SSA) (SSA-II).

I. INTRODUCTION

THE DOPPLER behaviors of backscattered echoes reflect the distribution of the line-of-sight velocity of the scatterers. The study of the Doppler properties of electromagnetic echoes backscattered from time-varying oceanic surfaces is of practical importance in a number of research areas such as sea-surface wind retrieving, sea-wave monitoring, and oceanic-surface current measuring. The Doppler shift, which is an important parameter of the Doppler spectrum, corresponds to a power-weighted mean line-of-sight velocity of the scatterers. However, the bandwidth of the Doppler spectrum is determined by the variance of the velocity distribution of the scattering facets at the sea surface. In [1] and [2], for the case of moderate-grazing angles and low-grazing angles (LGAs), the

Doppler spectra calculations based on the two-scale scattering method (TSM) and the comparison with experimental data are reported. Unfortunately, if the incident angle is smaller than 20° , the Doppler shifts predicted by TSM are insufficient for the reason that the Bragg scattering mechanism is invalid. In [3], Doppler shifts of backscattered fields from sea surfaces were predicted by asymptotic electromagnetic wave scattering theories (including Kirchhoff, first-order small-slope, and local-curvature approximations). As pointed out in [3], the predicted Doppler shifts for Kirchhoff and first-order small-slope approximations (SSAs) in copolarized configuration are insensitive to the polarization state. On the other hand, the local-curvature solutions yield significant differences between copolarized predicted Doppler shifts. In [4]–[6], the spectral properties of microwave backscattered signal from 1-D linear and nonlinear time-varying oceanic surfaces have been studied by utilizing the accelerated numerical techniques based on MoM. Just as the authors pointed out, the numerical simulations show an obvious broadening of the bandwidth for nonlinear surfaces at LGAs and a separation of the vertical and horizontal polarization spectra for nonlinear surfaces. In [5] and [6], Johnson *et al.* further investigated the influences of the hydrodynamic models on the Doppler spectra of L-band backscattered fields. Here, the recent work of Soriano *et al.* should also be mentioned [7]. At L-band, Doppler spectra from 2-D linear and nonlinear time-varying oceanic surfaces are investigated on the basis of a so-called small-slope integral equation method. To improve the implementation speed, in this paper, the nonlinear Creamer surface [8] is replaced by a Creamer(2) model in which the third- and higher order terms of the series expansion of Creamer surface representation are neglected. From the numerical results, they pointed out that the Doppler spectra corresponding to the nonlinear Creamer (2) surface are somewhat smoother and broader.

The SSA [9], which allows calculation of both a basic approximation of the theory (SSA-I) and second-order corrections to it (SSA-II), represents a systematic expansion of a scattering amplitude (SA) with respect to slopes of rough surface. The SSA has been successfully applied to evaluate electromagnetic scattering from sea surfaces [10]–[13]. In this paper, SSA-II is used to predict the Doppler shifts of backscattered fields from the composite sea surfaces for various radar frequencies and wind speeds. At the same time, a formula of the spectrum bandwidth is also derived utilizing TSM. In Section II, the outlines of the sea-surface model are described. According to the concept of the basic composite surface model [1], [14], [15], the sea-surface elevation is represented as a superposition of large-scale gravity waves and small-scale ripples. Here, in the

Manuscript received October 10, 2009; revised January 9, 2010, March 17, 2010, May 22, 2010, and July 30, 2010; accepted August 14, 2010. Date of publication October 4, 2010; date of current version February 25, 2011. This work was supported in part by the Young Scientists Fund of the National Natural Science Foundation of China under Grant 40906088 and in part by the Specialized Research Fund for the Doctoral Program of Higher Education.

The authors are with the Ocean University of China, Qingdao 266003, China (e-mail: wyh78917@yahoo.com.cn; zhangyanmin79@163.com).

Digital Object Identifier 10.1109/TGRS.2010.2070071

large-scale gravity-wave model, the horizontal displacement of particles on the long waves has been taken into account. On the other hand, we also assume that the small-scale roughness superimposed on the large-scale component is statistically independent with the large-scale one. Section III presents the asymptotic solutions to define Doppler frequency and Doppler bandwidth, while Section IV is devoted to the results and the comments. This paper ends with Section V for concluding remarks and perspectives.

II. COMPOSITE-SEA-SURFACE MODEL

Using a Cartesian coordinate system where \hat{x} is coincident with the wind direction, let $z(x, t)$ and $\varphi(x, t)$ denote the oceanic surface elevation and the scalar velocity potential, respectively. Under the condition of the first-order approximation, it is obtained that [16]

$$\begin{cases} \nabla^2 \varphi = 0, & d \leq 0 \\ \frac{\partial z}{\partial t} - \frac{\partial \varphi}{\partial d} = 0, & d = 0 \\ gz + \frac{\partial \varphi}{\partial d} = 0, & d = 0 \end{cases} \quad (1)$$

with $(\partial \varphi / \partial d) \rightarrow 0$ when $d \rightarrow -\infty$. Here, d denotes the water depth of the particles, and g is the gravity acceleration constant. From (1), the first-order solutions appropriate to a random homogeneous wave field are in the form

$$z_{\text{line}}(x, t) = \sum_{i=1}^N A_i \cos(K_i x - \omega_i t + \varphi_i) \quad (2)$$

$$\varphi(x, t) = \sum_{i=1}^N \frac{\omega_i A_i}{K_i} \exp(K_i d) \sin(K_i x - \omega_i t + \varphi_i) \quad (3)$$

with

$$A_i = \sqrt{2W(K_i)\Delta K_i} \quad (4)$$

where ΔK_i denotes the discrete intervals of wavenumber and spatial wavenumber $K_i = i\Delta K_i$, with an angular frequency $\omega_i = \sqrt{gK_i}$. Moreover, $W(K) = (\alpha/2|K|^3) \exp\{-(\beta g^2/K^2 U^4)\}$ is the Pierson-Moskowitz spectrum for 1-D sea surface [4], [5], and the constants are $\alpha = 0.0081$ and $\beta = 0.74$. U is the wind speed at a height of 19.5 m. In (2) and (3), φ_i represents a random phase uniformly distributed over the interval $(0, 2\pi)$. Using (3), the velocity field $(U(x, t), V(x, t))$ of the particles is obtained as

$$\begin{cases} U(x, t) = \frac{\partial \varphi}{\partial x} = \sum_{i=1}^N \omega_i A_i \exp(K_i d) \cos(K_i x - \omega_i t + \varphi_i) \\ V(x, t) = \frac{\partial \varphi}{\partial d} = \sum_{i=1}^N \omega_i A_i \exp(K_i d) \sin(K_i x - \omega_i t + \varphi_i). \end{cases} \quad (5)$$

In (3) and (5), d is the vertical coordinate and the positive direction is from the water to the air. Let r_l denote the deviation of a particle from its equilibrium position (x_0, z_0) . If only

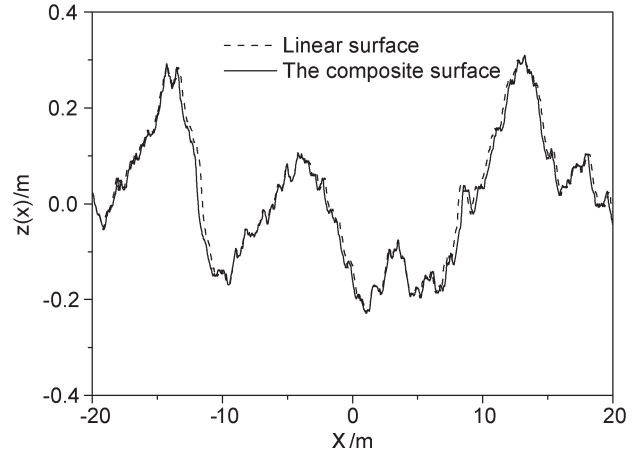


Fig. 1. Comparison of sea-surface profiles.

large-scale sea waves are considered, generally, $K_i r_l$ is a small quantity. Thus, (5) can be approximately rewritten as

$$\begin{cases} U_l(x, t) = \sum_{i=1}^{N_l} \omega_i A_i \exp(K_i z_0) \cos(K_i x_0 - \omega_i t + \varphi_i) \\ V_l(x, t) = \sum_{i=1}^{N_l} \omega_i A_i \exp(K_i z_0) \sin(K_i x_0 - \omega_i t + \varphi_i) \end{cases} \quad (6)$$

where the subscript l represents the large-scale waves. Therefore, by integration, we can obtain the large-scale gravity-wave model as

$$\begin{cases} z_l(x, t) = \sum_{i=1}^{N_l} A_i \cos(K_i x_0 - \omega_i t + \varphi_i) \\ x(x_0, t) = x_0 - \sum_{i=1}^{N_l} A_i \sin(K_i x_0 - \omega_i t + \varphi_i). \end{cases} \quad (7)$$

It should be pointed out that z_0 is set to be zero because only the particles on the sea surface are considered. Comparing (7) with the so-called ‘‘Choppy wave model’’ proposed by Noguier *et al.* in [17], one can find that they are coincident with each other.

Because the small scattering facets which ride on the large-scale waves move with the long-wave orbit velocity, the small-scale roughness can be simulated by

$$z_s(x, t) = \sum_{i=N_l+1}^N A_i \cos(K_i x_0 - \omega_i t + \varphi_i) \quad (8)$$

where the subscript s represents the small-scale waves. Using (7) and (8), the composite sea surface can be modeled as

$$z(x, t) = z_l(x, t) + z_s(x, t). \quad (9)$$

In this composite-sea-surface model, we only consider the horizontal displacement of particles induced by large-scale waves, and this differs from the Choppy wave model.

A comparison of sea-surface profiles is shown in Fig. 1. Here, the wind speed is 5 m/s. From the comparison, it is found that the profile shape of the composite sea surface shows the vertical skewness of sea waves, which are sharper at the crest and flatter

at the trough than linear waves. This property of the composite-sea-surface model is more consistent with the actual sea waves [8].

III. DOPPLER SHIFT AND BANDWIDTH

A. Doppler Shift

In this section, Doppler shifts of backscattered fields at small and moderate incidence angles are derived using the second-order SSA method. Considering a plane wave illuminating upon a 1-D sea surface, the SA $S(\vec{k}, \vec{k}_0)$ in the framework of SSA-II can be expressed as [10]

$$S(k_{sx}, k_{ix}) = 2 \frac{(k_{sz} k_{iz})^{1/2}}{k_{sz} + k_{iz}} \times \int \frac{dx}{2\pi} \exp[j(k_{ix} - k_{sx})x + j(k_{sz} + k_{iz})z(x, t)] \times \left(B(k_{sx}, k_{ix}) - \frac{j}{4} \int M(k_{sx}, k_{ix}\xi) \hat{z}(\xi) \times \exp(j\xi x) d\xi \right) \quad (10)$$

where $\hat{z}(\xi) \propto \sqrt{\widetilde{W}(K)}$ is the Fourier transform of $z(x, t)$ and $\widetilde{W}(K)$ denotes the sea-surface spectrum of $z(x, t)$ and can be written as [17]

$$\widetilde{W}(K) = W(K) + W_2(K) \quad (11)$$

where $W_2(K)$ presents a second-order corrective term. On the other hand, in (10), the second-order term $-(j/4) \int M(k_{sx}, k_{ix}; \xi) \hat{z}(\xi) \exp(j\xi x) d\xi$ represents a second-order small correction to the result of SSA-I; the x -coordinate is given by (7). Just as shown in Fig. 1, the horizontal displacement of particles on the long waves is usually small. Then, if the third- and higher order corrections to the results of SSA-I are neglected, the second-order correction term can be approximately rewritten as

$$-\frac{j}{4} \int M(k_{sx}, k_{ix}\xi) \hat{z}(\xi) \exp(j\xi x) d\xi \approx -\frac{j}{4} \int M(k_{sx}, k_{ix}\xi) \hat{z}'(\xi) \exp(j\xi x_0) d\xi \quad (12)$$

where $\hat{z}'(\xi)$ denotes the Fourier transform of linear sea-surface roughness.

Using the aforementioned approximation and substituting (7) and (9) into (10), the expression for $S(k_{sx}, k_{ix})$ from the composite sea surface is obtained as

$$S(k_{sx}, k_{ix}) \approx \frac{2(k_{sz} k_{iz})^{1/2}}{k_{sz} + k_{iz}} \times \int \frac{dx_0}{2\pi} \exp[j(k_{ix} - k_{sx})x_0 + j(k_{ix} - k_{sx})z_1(x_0, t) + j(k_{sz} + k_{iz})z'(x_0, t)] \times [1 - z_2(x_0, t)] \cdot \left(B(k_{sx}, k_{ix}) - \frac{j}{4} \int M(k_{sx}, k_{ix}\xi) \hat{z}'(\xi) \exp(j\xi x_0) d\xi \right) \quad (13)$$

with

$$z'(x_0, t) = \sum_{i=1}^N A_i \cos(K_i x_0 - \omega_i t + \varphi_i) \quad (14a)$$

$$z_1(x_0, t) = - \sum_{i=1}^{N_l} A_i \sin(K_i x_0 - \omega_i t + \varphi_i) \quad (14b)$$

$$z_2(x_0, t) = \sum_{i=1}^{N_l} K_i A_i \cos(K_i x_0 - \omega_i t + \varphi_i). \quad (14c)$$

To further simplify the calculations of (13), we perform the following transformation [18]:

$$B_{pq}(k_{sx}, k_{ix}) - \frac{j}{4} \int M_{pq}(k_{sx}, k_{ix}\xi) \hat{z}'(\xi) \exp(j\xi x_0) d\xi \approx B_{pq}(k_{sx}, k_{ix}) \times \exp \left[- \frac{j}{4B_{pp}(k_{sx}, k_{ix})} \int M_{pq}(k_{sx}, k_{ix}\xi) \hat{z}'(\xi) \times \exp(j\xi x_0) d\xi \right]. \quad (15)$$

The second term on the left-hand side of (15) represents a small correction to the first one; thus, such an approximation is legitimate. Substituting (15) into (13), we obtain

$$S(k_{sx}, k_{ix}) = \frac{(k_{sz} k_{iz})^{1/2}}{\pi(k_{sz} + k_{iz})} \times \int \exp[j(k_{ix} - k_{sx})x_0 + j(k_{ix} - k_{sx})z_1(x_0, t) + j(k_{sz} + k_{iz})z_0(x_0, t)] \times [1 - z_2(x_0, t)] dx_0 \quad (16)$$

where the modified roughness $z_0(x_0, t)$ can be expressed as

$$z_0(x_0, t) = \int \left\{ 1 - \frac{M_{pq}(k_{sx}, k_{ix}\xi)}{4(k_{sz} + k_{iz})B_{pp}(k_{sx}, k_{ix})} \right\} \times \hat{z}'(\xi) \exp(j\xi x_0) d\xi. \quad (17)$$

For Gaussian statistics of elevation $z'(x_0, t)$, the modified roughness $z_0(x_0, t)$ is also a Gaussian value. The expression for a scattering cross section is directly related to the second-order statistical moment of the SA, and the statistical evaluation mostly concerns (18), as shown at the bottom of the next page, where $x'_0 = x_0 + \Delta x_0$ and the superscript X^* stands for the conjugate quantity of X . Equation (18) contains ensemble averages of types

$$\begin{aligned} &\langle e^{j\alpha_1 X_1} e^{j\alpha_2 X_2} e^{j\alpha_3 X_3} e^{j\alpha_4 X_4} \rangle \\ &\langle e^{j\alpha_1 X_1} e^{j\alpha_2 X_2} e^{j\alpha_3 X_3} e^{j\alpha_4 X_4} X_5 \rangle \\ &\langle e^{j\alpha_1 X_1} e^{j\alpha_2 X_2} e^{j\alpha_3 X_3} e^{j\alpha_4 X_4} X_5 X_6 \rangle \end{aligned}$$

where X_1 – X_6 are zero-mean Gaussian random variables. Moreover, these ensemble averages can be found by utilizing [19]

$$\begin{aligned} & \langle e^{j\alpha_1 X_1} e^{j\alpha_2 X_2} e^{j\alpha_3 X_3} e^{j\alpha_4 X_4} \rangle \\ &= \exp \left[-\frac{1}{2} \sum_{i=1}^4 \sum_{k=1}^4 \alpha_i \alpha_k \rho_{ik} \right] \end{aligned} \quad (19a)$$

$$\begin{aligned} & \langle e^{j\alpha_1 X_1} e^{j\alpha_2 X_2} e^{j\alpha_3 X_3} e^{j\alpha_4 X_4} X_5 \rangle \\ &= -j \frac{\partial \langle e^{j\alpha_1 X_1} e^{j\alpha_2 X_2} e^{j\alpha_3 X_3} e^{j\alpha_4 X_4} e^{j\alpha_5 X_5} \rangle}{\partial \alpha_5} \bigg|_{\alpha_5=0} \end{aligned} \quad (19b)$$

$$\begin{aligned} & \langle e^{j\alpha_1 X_1} e^{j\alpha_2 X_2} e^{j\alpha_3 X_3} e^{j\alpha_4 X_4} X_5 X_6 \rangle \\ &= -\frac{\partial \langle e^{j\alpha_1 X_1} e^{j\alpha_2 X_2} e^{j\alpha_3 X_3} e^{j\alpha_4 X_4} e^{j\alpha_5 X_5} e^{j\alpha_6 X_6} \rangle}{\partial \alpha_5 \partial \alpha_6} \bigg|_{\alpha_5=\alpha_6=0} \end{aligned} \quad (19c)$$

where $\rho_{ik} = \langle X_i X_k^* \rangle$ denotes the correlation functions. In the following, to simplify the notations, in the correlation function expression, Δx_0 and Δt are replaced by x_0 and t , respectively.

To express the correlation functions as functions of the time from a given state, we will consider only very short time lags, i.e., $|t| \ll 1.0$ s. For example, to analyze the statistics of the phase of the microwave signal returning from the sea surface, the time lags should be less than 0.01 s at X-band and 0.003 s at Ka-band [20]. Thus, we can perform a Taylor expansion around zero at first order to describe the changes of the correlation functions during this small time lag, i.e.,

$$\rho_{ik}(x_0, t) \approx \rho_{ik}(x_0, 0) + t \frac{\partial \rho_{ik}(x_0, t)}{\partial t} \bigg|_{t=0} + \dots \quad (20)$$

Using (18)–(20), the final results after some lengthy but straightforward mathematical manipulations are given by

$$\sigma_{pq}(t) = \sigma_{pq}^0(0) + \sigma_{pq}^1(t) \quad (21)$$

where

$$\begin{aligned} \sigma_{pq}^0(0) &= \left(\frac{2k_{iz}k_{sz}}{(k_{iz} + k_{sz})\pi} B_{pq} \right)^2 \\ &\times \int b10 \times (1 + a10) \\ &\times \exp[j(k_{ix} - k_{sx})x_0] dx_0 \end{aligned} \quad (22a)$$

$$\begin{aligned} \sigma_{pq}^1(t) &= t \times \sigma_{pq}^1(0) \\ &= t \times \left(\frac{2k_{iz}k_{sz}}{(k_{iz} + k_{sz})\pi} B_{pq} \right)^2 \\ &\times \int [b11 \times (1 + a10) + b10 \times a11] \\ &\times \exp[j(k_{ix} - k_{sx})x_0] dx_0 \end{aligned} \quad (22b)$$

with

$$\begin{aligned} b10 &= \exp \{ (k_{ix} - k_{sx})^2 [\rho_{11}(x_0, 0) - \rho_{11}(0, 0)] \\ &+ (k_{ix} - k_{sx}) \cdot (k_{sz} + k_{iz}) \\ &\times [\rho_{01}(x_0, 0) + \rho_{*01}(-x_0, 0) \\ &- \rho_{01}(0, 0) - \rho_{*01}(0, 0)] \\ &+ (k_{iz} + k_{sz})^2 [\rho_{00}(x_0, 0) - \rho_{00}(0, 0)] \} \end{aligned} \quad (23a)$$

$$\begin{aligned} b11 &= b10 \times \{ (k_{ix} - k_{sx})^2 \tilde{\rho}_{11}(x_0, 0) \\ &+ (k_{ix} - k_{sx}) \cdot (k_{sz} + k_{iz}) \\ &\times [\tilde{\rho}_{01}(x_0, 0) + \tilde{\rho}_{*01}(-x_0, 0)] \\ &+ (k_{iz} + k_{sz})^2 \tilde{\rho}_{00}(x_0, t) \} \end{aligned} \quad (23b)$$

$$\begin{aligned} & \langle S(k_{sx}, k_{ix}) S^*(k_{sx}, k_{ix}) \rangle \\ &= \frac{k_{sz}k_{iz}}{\pi^2(k_{sz} + k_{iz})^2} \left\{ \int \exp[j(k_{ix} - k_{sx})\Delta x_0] \langle \exp \{ j(k_{ix} - k_{sx}) [z_1(x'_0, t + \Delta t) - z_1(x_0, t)] \right. \\ &\quad \left. + j(k_{sz} + k_{iz}) [z_0(x'_0, t + \Delta t) - z_0^*(x_0, t)] \} \rangle dx'_0 dx_0 \right. \\ &\quad - \int \exp[j(k_{ix} - k_{sx})\Delta x_0] \langle \exp \{ j(k_{ix} - k_{sx}) [z_1(x'_0, t + \Delta t) - z_1(x_0, t)] \\ &\quad \left. + j(k_{sz} + k_{iz}) [z_0(x'_0, t + \Delta t) - z_0^*(x_0, t)] \} \rangle z_2(x'_0, t + \Delta t) \rangle dx'_0 dx_0 \right. \\ &\quad - \int \exp[j(k_{ix} - k_{sx})\Delta x_0] \langle \exp \{ j(k_{ix} - k_{sx}) [z_1(x'_0, t + \Delta t) - z_1(x_0, t)] \\ &\quad \left. + j(k_{sz} + k_{iz}) [z_0(x'_0, t + \Delta t) - z_0^*(x_0, t)] \} \rangle z_2(x_0, t) \rangle dx'_0 dx_0 \right. \\ &\quad \left. + \int \exp[j(k_{ix} - k_{sx})\Delta x_0] \langle \exp \{ j(k_{ix} - k_{sx}) [z_1(x'_0, t + \Delta t) - z_1(x_0, t)] \right. \\ &\quad \left. + j(k_{sz} + k_{iz}) [z_0(x'_0, t + \Delta t) - z_0^*(x_0, t)] \} \right. \\ &\quad \left. \times z_2(x'_0, t + \Delta t) z_2(x_0, t) \rangle dx'_0 dx_0 \right\} \end{aligned} \quad (18)$$

$$\begin{aligned}
a_{10} = & \rho_{22}(x_0, 0) - [-(k_{ix} - k_{sx})\rho_{12}(-x_0, 0) \\
& + (k_{iz} + k_{sz})(\rho_{02}(0, 0) - \rho *_{02}(x_0, 0))] \\
& \times [(k_{ix} - k_{sx})\rho_{12}(x_0, 0) \\
& + (k_{iz} + k_{sz})(\rho_{02}(x_0, 0) - \rho *_{02}(0, 0))] \\
& + j \{-2(k_{ix} - k_{sx})\rho_{12}(x_0, 0) - (k_{sz} + k_{iz}) \\
& \times [\rho_{02}(x_0, 0) - \rho *_{02}(x_0, 0) \\
& + \rho_{02}(0, 0) - \rho *_{02}(0, 0)]\} \quad (23c)
\end{aligned}$$

$$\begin{aligned}
a_{11} = & \tilde{\rho}_{22}(x_0, 0) - [-(k_{ix} - k_{sx})\tilde{\rho}_{12}(-x_0, 0) \\
& - (k_{iz} + k_{sz})\tilde{\rho} *_{02}(x_0, 0)] \\
& \times [(k_{ix} - k_{sx})\tilde{\rho}_{12}(x_0, 0) - (k_{iz} + k_{sz})\tilde{\rho}_{02}(x_0, 0)] \\
& + j \{-2(k_{ix} - k_{sx})\tilde{\rho}_{12}(x_0, 0) - (k_{sz} + k_{iz}) \\
& \times [\tilde{\rho}_{02}(x_0, 0) - \tilde{\rho} *_{02}(x_0, 0)]\} \quad (23d)
\end{aligned}$$

$$\tilde{\rho}(x_0, 0) = \left. \frac{\partial \rho(x_0, t)}{\partial t} \right|_{t=0}. \quad (23e)$$

Under the condition of a small time lag, i.e., $|t| \ll 1.0$ s, we have

$$\begin{aligned}
\sigma_{pq}(t) &= \sigma_{pq}^0(0) \left[\frac{|\sigma_{pq}^0(0)|^2 + t \times \sigma_{pqr}^{\prime 1}(0)\sigma_{pqr}^0(0) + t \times \sigma_{pqi}^{\prime 1}(0)\sigma_{pqi}^0(0)}{|\sigma_{pq}^0(0)|^2} \right. \\
&\quad \left. + j \frac{\sigma_{pqi}^{\prime 1}(0)\sigma_{pqr}^0(0) - \sigma_{pqr}^{\prime 1}(0)\sigma_{pqi}^0(0)}{|\sigma_{pq}^0(0)|^2} \times t \right] \\
&\approx \sigma_{pq}^0(0) \exp \left[j \frac{\sigma_{pqi}^{\prime 1}(0)\sigma_{pqr}^0(0) - \sigma_{pqr}^{\prime 1}(0)\sigma_{pqi}^0(0)}{|\sigma_{pq}^0(0)|^2} t \right] \quad (24)
\end{aligned}$$

where $\sigma_{pqr}^0(t)$, $\sigma_{pqi}^0(t)$ and $\sigma_{pqr}^{\prime 1}(t)$, $\sigma_{pqi}^{\prime 1}(t)$ denote the real and the imaginary part of $\sigma_{pq}^0(t)$ and $\sigma_{pq}^{\prime 1}(t)$, respectively.

The introduction of a time-dependent phase term leads to the definition of a mean Doppler shift f_D induced by the distributed sea-surface motions. Transforming the normalized radar cross section from time to frequency domain, we have $\sigma_{\alpha\alpha}(f_D)$, as shown in (25) at the bottom of the page.

In order to ensure $t \ll 1.0$ s, we should set $T \ll 1.0$ s. By integration, it is obtained that $\sigma_{\alpha\alpha}(f_D)$ is denoted in (26), as shown at the bottom of the page, where $\sin c(x) = \sin(x)/x$.

From (26), by setting $2\pi f_D - (\sigma_{\alpha\alpha i}^{\prime 1}(0)\sigma_{\alpha\alpha r}^0(0) - \sigma_{\alpha\alpha r}^{\prime 1}(0)\sigma_{\alpha\alpha i}^0(0)/|\sigma_{\alpha\alpha}^0(0)|^2) = 0$, the Doppler shift f_D , i.e., the spectral centroid, is obtained as

$$f_D = \frac{1}{2\pi} \frac{\sigma_{\alpha\alpha i}^{\prime 1}(0)\sigma_{\alpha\alpha r}^0(0) - \sigma_{\alpha\alpha r}^{\prime 1}(0)\sigma_{\alpha\alpha i}^0(0)}{|\sigma_{\alpha\alpha}^0(0)|^2}. \quad (27)$$

B. Spectrum Bandwidth

In this section, a formula of the spectrum bandwidth for the scattered echoes from the composite sea surface is presented on the basis of the TSM. Doppler bandwidth f_δ can be defined by the following [2], [21]:

$$f_\delta^2 = \frac{\int (f' - f_D)^2 S(f') df'}{\int S(f') df'} \quad (28)$$

where f_D is the Doppler shift, f' denotes the Doppler frequency of scattered field from each surface element, and $S(f')$ is the Doppler spectrum. Introducing the concept of the probability density function (Pdf), (28) can be rewritten as

$$f_\delta^2 = \int (f' - f_D)^2 P(f') df' \quad (29)$$

where the Pdf $P(f') = (S(f')/\int S(f'')df'')$.

Let $f' = f_D + \Delta f$. Thus, we can obtain the following:

$$f_\delta^2 = \int \Delta f^2 P(f') df' = \langle \Delta f \Delta f^* \rangle. \quad (30)$$

Here, Δf which is induced by orbit motion is the dispersed Doppler frequency around f_D . For the composite sea surface used in our work, the orbit velocity has been given by (6), and then, it is obtained that

$$\Delta f = \frac{k}{\pi} (U_t(x, t) \sin \theta_i + V_t(x, t) \cos \theta_i) \quad (31)$$

where $k = 2\pi/\lambda$ and λ denotes the wavelength of the electromagnetic wave.

Substituting (31) into (30), the bandwidth of the Doppler spectrum can be expressed by (32), as shown at the bottom of the next page.

$$\sigma_{\alpha\alpha}(f_D) = \sigma_{\alpha\alpha}^0(0) \int_{-T/2}^{T/2} \exp \left\{ j \left[\frac{\sigma_{\alpha\alpha i}^{\prime 1}(0)\sigma_{\alpha\alpha r}^0(0) - \sigma_{\alpha\alpha r}^{\prime 1}(0)\sigma_{\alpha\alpha i}^0(0)}{|\sigma_{\alpha\alpha}^0(0)|^2} - 2\pi f_D \right] t \right\} dt \quad (25)$$

$$\sigma_{\alpha\alpha}(f_D) = \sigma_{\alpha\alpha}^0(0) T \sin c \left\{ \left(2\pi f_D - \frac{\sigma_{\alpha\alpha i}^{\prime 1}(0)\sigma_{\alpha\alpha r}^0(0) - \sigma_{\alpha\alpha r}^{\prime 1}(0)\sigma_{\alpha\alpha i}^0(0)}{|\sigma_{\alpha\alpha}^0(0)|^2} \right) T \right\} \quad (26)$$

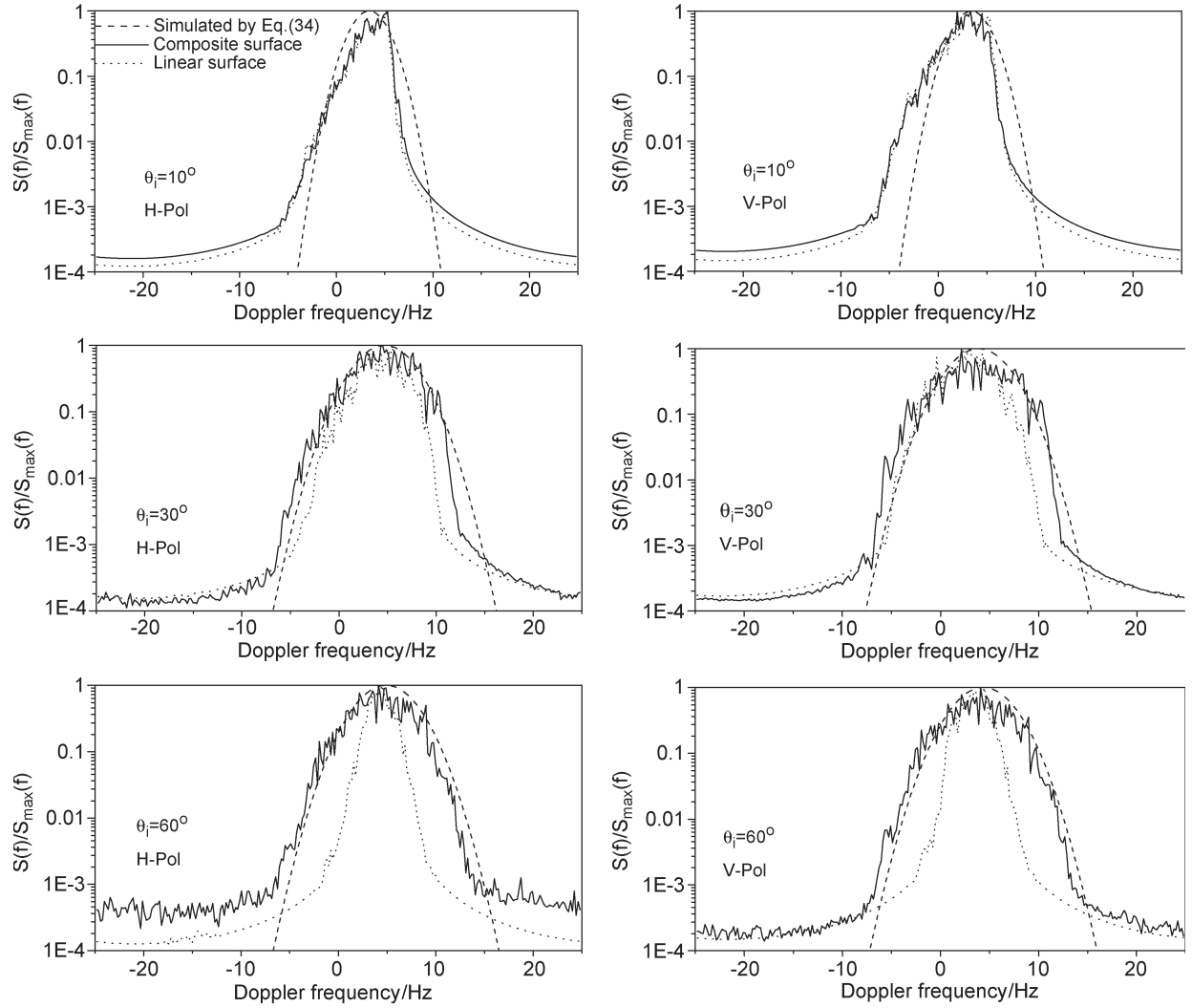


Fig. 2. Comparison of the average Doppler spectra corresponding to backscattering from linear and composite surfaces at radar frequency of 1.3 GHz (L-band). Dashed, solid, and dotted lines correspond to the spectrum model (34), composite sea surface, and linear sea surface, respectively. The spectra are normalized to their respective maximum values.

It should be pointed out that the integrations in (32) include only the “long-wave” part of the sea-surface spectrum $W(K)$. K_L denotes the cutoff wavenumber [22], and σ_v is the root-mean-square of the orbit velocity.

In (10), if the time-varying sea surface $z(x, t)$ is simulated by (2) instead of (9), then, in (16), the terms $j(k_{ix} - k_{sx})z_1(x_0, t)$ and $z_2(x_0, t)$ will disappear. However, $j(k_{ix} - k_{sx})z_1(x_0, t)$ reflects the effect of the horizontal component of the orbital

$$\begin{aligned}
 f_\delta &= \sqrt{\langle \Delta f \Delta f^* \rangle} \\
 &= \sqrt{\frac{k^2}{\pi^2} \left\langle \left\{ \sin \theta_i \sum_i^{N_i} \omega_i A_i \cos(K_i x_0 - \omega_i t + \varphi_i) \right\}^2 + \left\{ \cos \theta_i \sum_i^{N_i} \omega_i A_i \sin(K_i x_0 - \omega_i t + \varphi_i) \right\}^2 \right.} \\
 &\quad \left. + 2 \sin \theta_i \cos \theta_i \sum_i^{N_i} \omega_i A_i \cos(K_i x_0 - \omega_i t + \varphi_i) \sum_i^{N_i} \omega_i A_i \sin(K_i x_0 - \omega_i t + \varphi_i) \right\rangle} \\
 &= \frac{k}{\pi} \sqrt{\int_0^{K_L} \omega^2 W(K) dK} \\
 &= \frac{k}{\pi} \sigma_v
 \end{aligned} \tag{32}$$

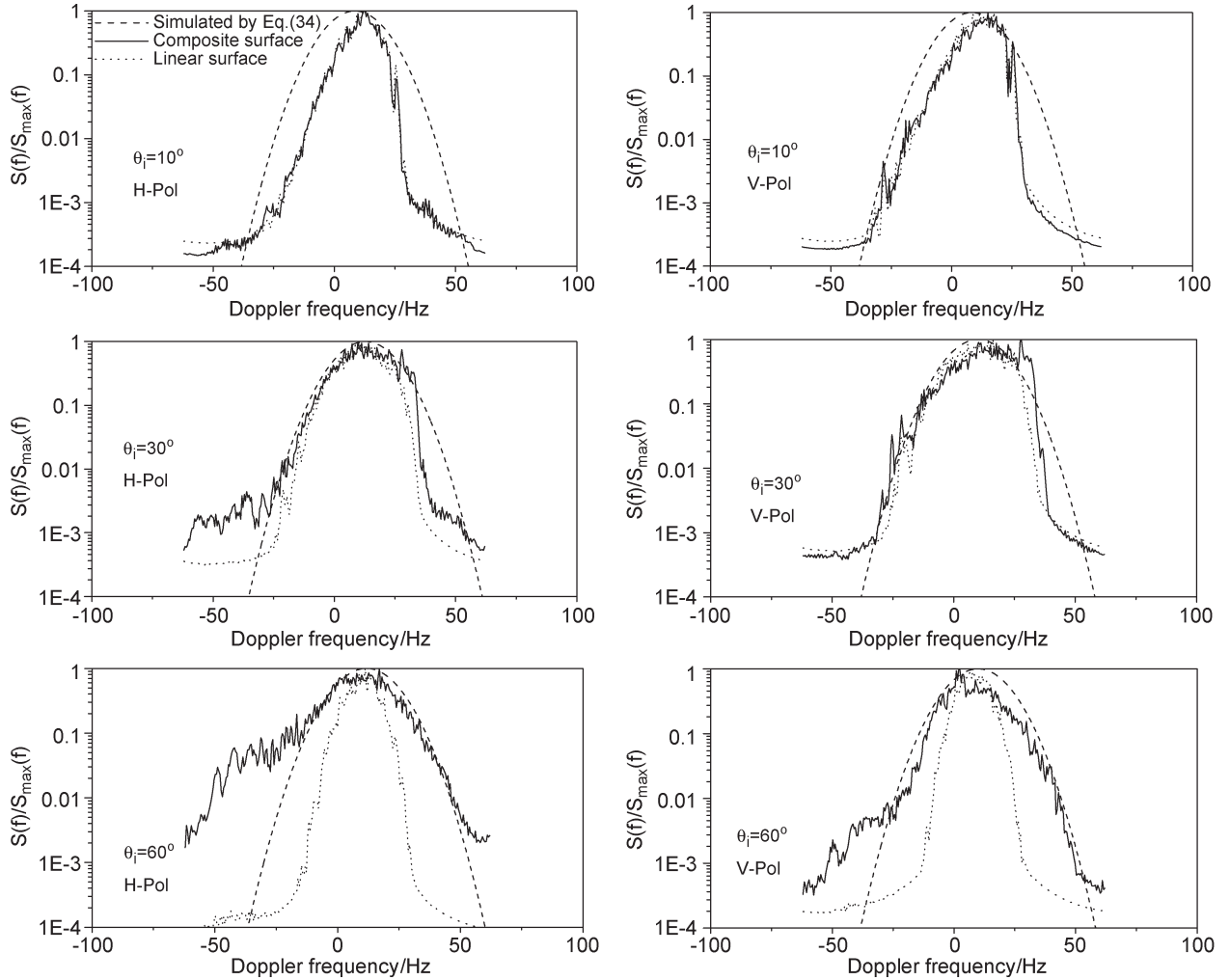


Fig. 3. Same as in Fig. 2 but the radar frequency is 5.3 GHz (C-band).

velocity on the Doppler shift (or spectral bandwidth). Thus, if the linear surface model, in which the horizontal displacement of particles on the long waves cannot be taken into account, is utilized to simulate the sea surface, we can obtain the spectrum bandwidth f'_δ as

$$f'_\delta = \frac{k}{\pi} \sigma_v \cos \theta_i. \quad (33)$$

Supposing the Doppler spectrum has a Gaussian shape, we can obtain the spectrum model as

$$S(f) = \frac{\sigma_{\alpha\alpha}^0(0)}{\sqrt{2\pi}f_\delta^2} \exp \left\{ -\frac{(f - f_D)^2}{2f_\delta^2} \right\} \quad (34)$$

where the Doppler shift f_D and the bandwidth f_δ can be calculated by (27) and (32), respectively.

IV. NUMERICAL RESULTS

In this section, we start with the comparison between the average Doppler spectra (40 time-evolving surface realizations) simulated by the Monte Carlo SSA-II method and the ap-

proximation results of (34). Figs. 2 and 3 show such comparison at a wind speed of 5 m/s. At small incidence angles, the Doppler spectra of signals backscattered from linear and composite sea surfaces are in good agreement with each other. This is because, at small incidence angles, the bandwidth of the Doppler spectrum will not be affected by the horizontal component of orbit velocity. Figs. 2 and 3 also show that the bandwidths of the spectra simulated by the Monte Carlo SSA-II method are somewhat narrower than the approximation results (34) when the incident angle is small. The reason for this phenomenon is that, at small incident angles, the scattered fields are mainly induced by the specular reflected fields and the spectral bandwidths of the backscattered signals are determined by the orbit velocities of the specular scattering points. However, the bandwidth of the approximate spectrum model is derived by TSM, and it is determined by the orbit velocities of all small scattering facets. Thus, the bandwidth of the approximate spectrum model will be somewhat wider than the directly simulated results by the Monte Carlo SSA-II method. At larger incidence angles, the Doppler spectra simulated by (34) fit the Monte Carlo results corresponding to composite sea surface better. The Monte Carlo spectra for linear sea surface are obviously narrower than the approximate

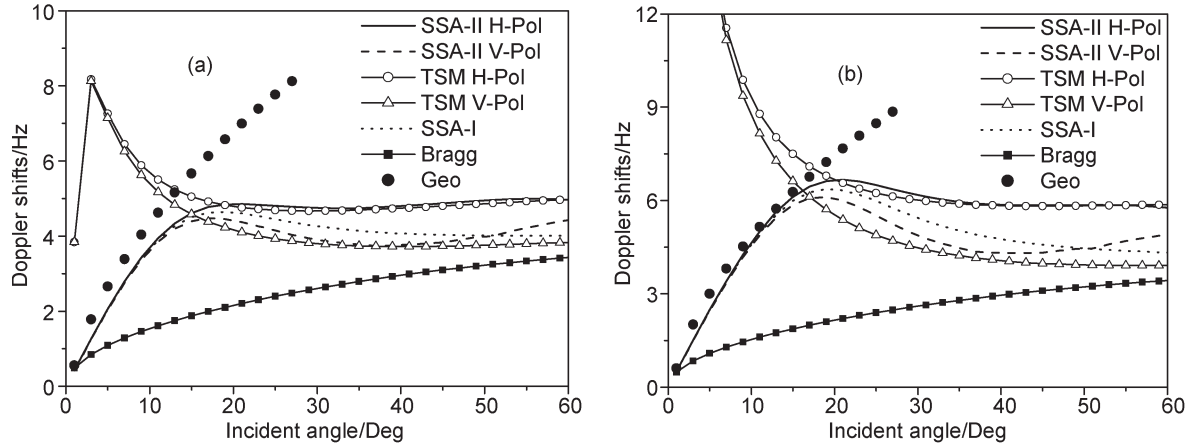


Fig. 4. Doppler shifts at L-band by different methods. (a) Wind speed is 5 m/s. (b) Wind speed is 8 m/s.

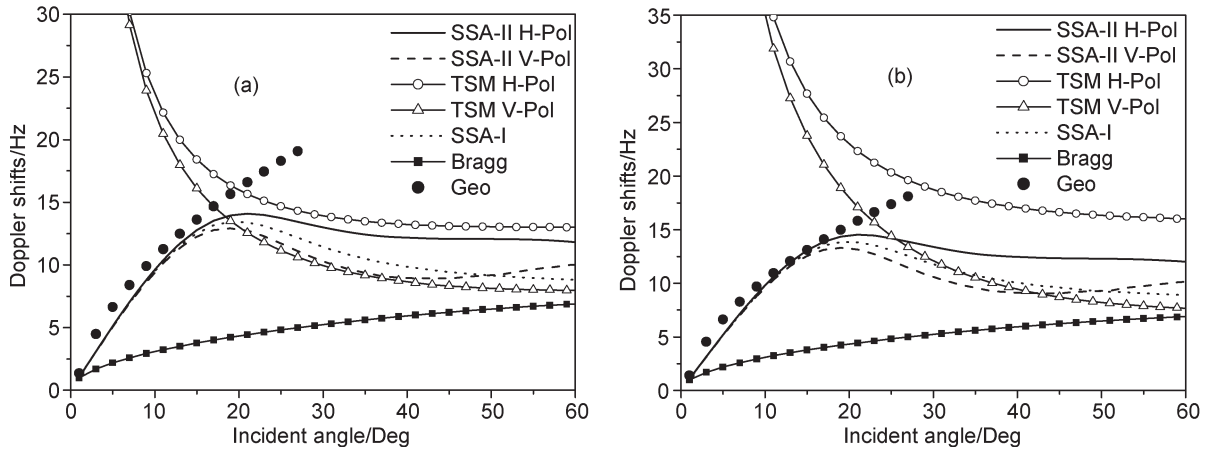


Fig. 5. Doppler shifts at C-band by different methods. (a) Wind speed is 5 m/s. (b) Wind speed is 8 m/s.

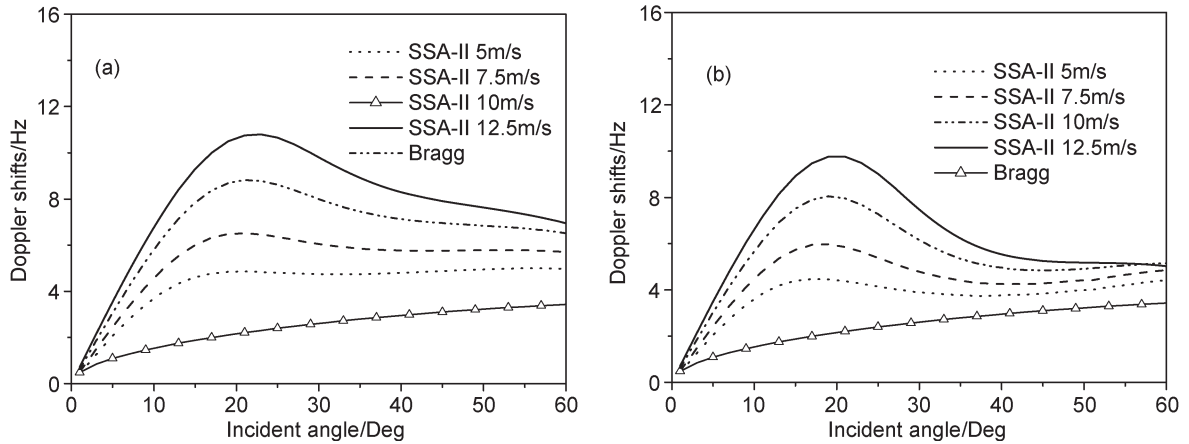


Fig. 6. Doppler shifts versus incident angle for different wind speeds. (a) HH polarization (b) VV polarization.

spectrum model. This is because the horizontal displacements of scattering facets are not taken into account in the linear model and the horizontal components of orbit velocities cannot be considered.

In Figs. 4 and 5, the Doppler shifts are evaluated as a function of incident angle for different wind speeds in the upwind configuration. The microwave wavelengths in Figs. 4 and 5 are 23 cm (L-band) and 5.7 cm (C-band), respectively. The TSM

[2], SSA-I, Bragg [4], [23], and geometrical optics (GO) [24] results are also presented for comparisons. Here, the Doppler shifts associated to the resonant Bragg waves and the so-called long waves in GO are both evaluated by

$$f_D(\theta_i) = \bar{v} \frac{k \sin \theta_i}{\pi} \quad (35)$$

where \bar{v} denotes the mean sea-surface horizontal velocity.

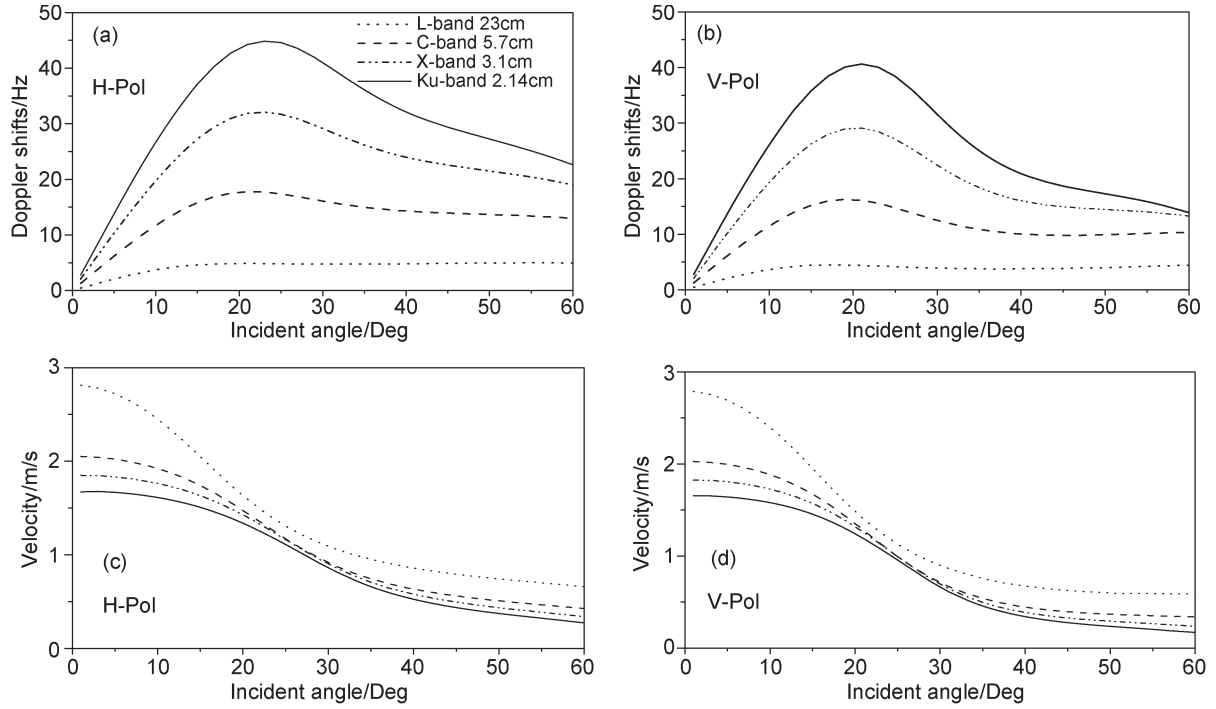


Fig. 7. (a)–(b) Doppler shifts versus incident angle for different radar frequencies. (c)–(d) Sea-surface horizontal velocity predicted by Doppler shift at various radar frequencies.

For the resonant Bragg waves [4]

$$\bar{v} = \sqrt{\frac{g}{2k \sin \theta_i}}. \quad (36)$$

For GO approximation, the mean velocity is evaluated by [24]

$$\bar{v} = \frac{\int_0^{K_L} \omega K W(K) dK}{\int_0^{K_L} K^2 W(K) dK}. \quad (37)$$

From Figs. 4 and 5, it is found that Doppler shifts predicted by SSA-I, SSA-II, and TSM increase with wind speed. However, the results obtained by the Bragg resonant theory are wind speed independent. The predicted Doppler shifts for SSA-I and Bragg resonant theory in copolarized configuration are insensitive to the polarization state. Nevertheless, the SSA-II and TSM results yield significant differences between copolarized predicted Doppler frequencies, and the predicted Doppler shifts are always larger in HH polarization than in VV polarization. The reason is that, for the case of upwind configuration, at the regions where the slopes of the so-called long tilting waves are positive, Doppler shifts of scattered fields from small scattering facets include additional Doppler frequencies due to orbit motions and the radar signals are more sensitive to surface slope in HH polarization than in VV. This effect is commonly called the tilt modulation. From the comparisons between the SSA-II and TSM results, one can find that the Doppler shifts predicted by SSA-II are in agreement with those predicted by TSM at larger incidence angles ($> 20^\circ$) if the radar frequency or the wind speed is low. However, for the high-radar-frequency case, as shown in Fig. 5(b), the differences between SSA-II and TSM solutions are noticeable. The possible reason is that the

approximation used in (15) is invalid when the wind speed and radar frequency are both higher. On the other hand, for small incident angles ($< 20^\circ$), the Bragg resonance theory is invalid and the TSM results are not reasonable. Fortunately, from the comparisons between the SSA-I/II and GO results, we can get an impression that acceptable results can be obtained by SSA-I/II. From the figures, one can see that SSA results first rapidly increase from zero hertz at nadir to a maximum around 18° and then decrease.

In Fig. 6, Doppler shifts predicted by SSA-II are presented at the radar frequency $f_R = 1.3$ GHz ($\lambda_R = 23$ cm) for different wind speeds. Fig. 6(a) corresponds to HH polarization, and Fig. 6(b) corresponds to VV polarization. From Fig. 6, it is obvious that the Doppler shifts increase with wind speed. At small incidence angles, the Doppler signal is dominated by the scattering from long waves. As the mean sea-surface horizontal velocity \bar{v} increases with wind speed [see (37)], the Doppler shift at these small incidence angles will depend on the wind speed sensitively. At larger incidence angles, the Bragg scattering plays a more important role in the scattering field. Although the Bragg shift does not depend on wind speed [see (36)], the orbit velocity of the long waves becomes larger with the increase of wind speed and the additional Doppler frequency due to the tilt modulation will become larger. Nevertheless, at larger incidence angles, the wind-speed dependence of Doppler shift is weaker.

In Fig. 7, we show the Doppler shifts as a function of the incident angle using SSA-II for four typical microwave wavelengths, i.e., L-band ($\lambda_R = 23$ cm), C-band ($\lambda_R = 5.7$ cm), X-band ($\lambda_R = 3.1$ cm), and Ku-band ($\lambda_R = 2.1$ cm). The wind speed is 5 m/s. Fig. 7(a), (c) and (b), (d) corresponds to HH and VV polarizations, respectively. As shown in Fig. 7(a) and (b), we can see that the Doppler shift increases with the

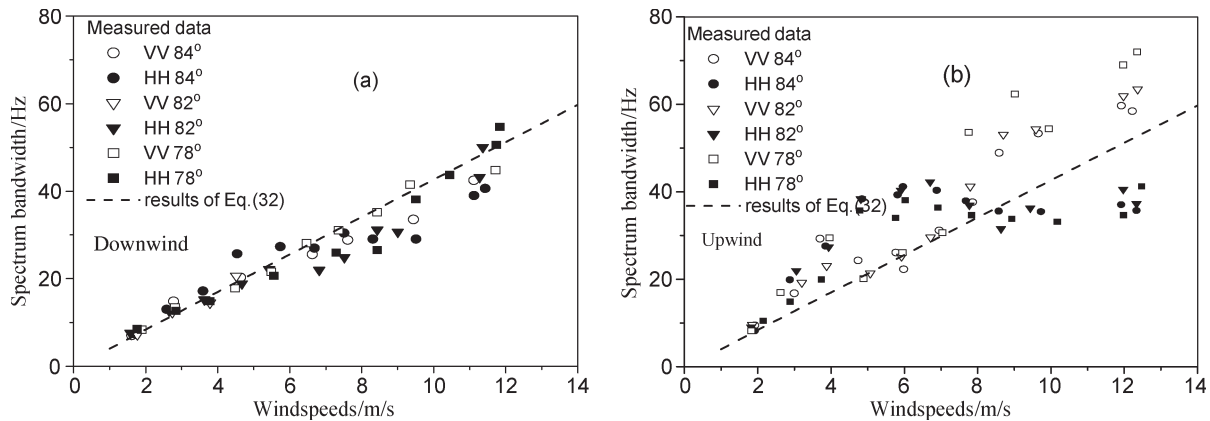


Fig. 8. Comparisons of the spectrum bandwidth versus wind speed between our results and the measured data. (a) Downwind. (b) Upwind.

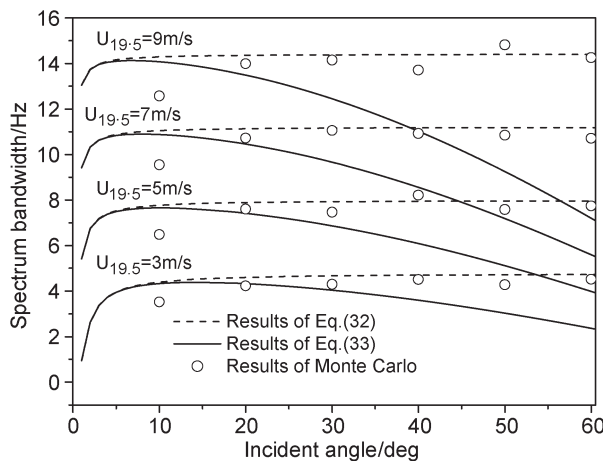


Fig. 9. Bandwidths versus incident angle for different wind speeds.

radar frequency. This indicates that the radar frequency has a significant impact on Doppler shift [see (35)]. Indeed, as radar frequency increases, the Doppler signal is more sensitive to smaller scales and, thus, to slower waves. In Fig. 7(c) and (d), we show the sea-surface horizontal velocity predicted by Doppler shift at various radar frequencies. Just as expected, the predicted velocity is lower at higher radar frequency.

In Fig. 8, the comparisons of the spectrum bandwidths versus wind speeds are shown between the present calculations with (32) and the measured data for both downwind and upwind observed directions [25]. The radar frequency is 14 GHz. Under the condition that the radar looking direction is in upwind or downwind, the Doppler spectrum bandwidth of backscattered fields from 1-D sea surface is equal to the result corresponding to that of the 2-D case. Therefore, the comparisons in Fig. 8 are of certain significance. From (32), one can note that the predicted bandwidth is not a function of the radar looking direction. Thus, the predicted results along downwind and upwind are the same. As shown in Fig. 8, the predicted results along downwind direction are consistent with the measured data. However, in the upwind direction, the results by (32) are somewhat smaller than the experimental data. This phenomenon may be caused by the actual wave's horizontal skewness, which is not considered in this paper. In Fig. 9, we plot the bandwidths as a function of the incident angles with different wind speeds

for C-band microwave. The dashed and solid lines denote the results predicted by (32) and (33), respectively; the circles denote the numerical simulated results by the Monte Carlo SSA-II method. It is shown that, as the incident angle increases, the bandwidths corresponding to the composite-sea-surface model increase first and then become almost a constant. However, the predicted results corresponding to the linear surface model first rapidly increase with incidence angle and then decrease. At small incidence angles, the differences between the dashed and solid lines are very small. However, the differences will increase rapidly with the increase of the incident angle. This is because the cosine function in (33) becomes smaller with the increase of incidence angle. From Fig. 9, one can also find that the Monte Carlo results are somewhat smaller than those predicted by (32) when the incident angle is smaller. The reason has been given in the paragraph following Fig. 3. At larger incidence angles, the predicted bandwidth by (32) can fit the Monte Carlo results much better than those corresponding to (33). Figs. 8 and 9 also show that the bandwidth increases with wind speed.

V. CONCLUSION

In this paper, time-dependent asymptotic solutions have been derived to predict Doppler shifts using SSA-II in connection with the composite-sea-surface model. At the same time, a formula of the spectrum bandwidth for the scattered echoes is also presented utilizing TSM. As shown, Doppler shifts will be dependent on radar frequency, wind speed, incident angle, and polarization. Doppler shifts increase with the radar frequency and wind speed. The results obtained from SSA-II and TSM can yield significant differences between copolarized predicted Doppler frequencies, and the predicted Doppler shifts are always larger in HH polarization than in VV polarization. At larger incidence angles, the Doppler shifts predicted by SSA-II are consistent with the TSM results. However, at low incidence angles ($< 20^\circ$), SSA-II results are more reasonable than those obtained by TSM. From the comparisons, we can conclude that reasonable results can be obtained by the formula presented in this paper.

Although this work is limited to the 1-D surface, the conclusions obtained in this paper will help to better understand

the radar frequency, incidence angle, wind speed, and polarization sensitivities of time-dependent sea-surface backscattered signals. Further work should be carried out to investigate the properties of Doppler spectra from 2-D sea surfaces.

ACKNOWLEDGMENT

The authors would like to thank the anonymous reviewers for providing valuable and constructive comments.

REFERENCES

- [1] V. U. Zavorotny and A. G. Voronovich, "Two-scale model and ocean radar Doppler spectra at moderate- and low-grazing angles," *IEEE Trans. Antennas Propag.*, vol. 46, no. 1, pp. 84–92, Jan. 1998.
- [2] R. Romeiser and D. R. Thompson, "Numerical study on the along-track interferometric radar imaging mechanism of oceanic surface currents," *IEEE Trans. Geosci. Remote Sens.*, vol. 38, no. 1, pp. 446–458, Jan. 2000.
- [3] A. A. Mouche, B. Chapron, N. Reul, and F. Collard, "Predicted Doppler shifts induced by ocean surface wave displacements using asymptotic electromagnetic wave scattering theories," *Waves Random Complex Media*, vol. 18, no. 1, pp. 185–196, Feb. 2008.
- [4] J. V. Toporkov and G. S. Brown, "Numerical simulations of scattering from time-varying randomly rough surfaces," *IEEE Trans. Geosci. Remote Sens.*, vol. 38, no. 4, pp. 1616–1625, Jul. 2000.
- [5] J. T. Johnson, J. V. Toporkov, and G. S. Brown, "A numerical study of backscattering from time-evolving sea surfaces: Comparison of hydrodynamic models," *IEEE Trans. Geosci. Remote Sens.*, vol. 39, no. 11, pp. 2411–2420, Nov. 2001.
- [6] A. R. Hayslip, J. T. Johnson, and G. R. Baker, "Further numerical studies of backscattering from time-evolving nonlinear sea surfaces," *IEEE Trans. Geosci. Remote Sens.*, vol. 41, no. 10, pp. 2287–2293, Oct. 2003.
- [7] G. Soriano, M. Joelson, and M. Saillard, "Doppler spectrum from two-dimensional ocean surface at L-band," *IEEE Trans. Geosci. Remote Sens.*, vol. 44, no. 9, pp. 2430–2437, Sep. 2006.
- [8] D. B. Creamer, F. Henyey, R. Schult, and J. Wright, "Improved linear representation of ocean surface waves," *J. Fluid Mech.*, vol. 205, pp. 135–161, 1989.
- [9] A. G. Voronovich, *Wave Scattering From Rough Surface*. Heidelberg, Germany: Springer-Verlag, 1994.
- [10] A. G. Voronovich and V. U. Zavorotny, "Theoretical model for scattering of radar signals in Ku and C-bands from a rough sea surface with breaking waves," *Waves Random Media*, vol. 11, no. 3, pp. 247–269, Jul. 2001.
- [11] J. V. Toporkov and G. S. Brown, "Numerical study of the extended Kirchhoff approach and the lowest order small slope approximation for scattering from ocean-like surfaces: Doppler analysis," *IEEE Trans. Antennas Propag.*, vol. 50, no. 4, pp. 417–425, Apr. 2002.
- [12] C. Bourlier, "Azimuthal harmonic coefficients of the microwave backscattering from a non-Gaussian ocean surface with the first-order SSA model," *IEEE Trans. Geosci. Remote Sens.*, vol. 42, no. 11, pp. 2600–2611, Nov. 2004.
- [13] T. Elfouhaily, S. Guignard, R. Awadallah, and D. R. Thompson, "Local and non-local curvature approximation: A new asymptotic theory for wave scattering," *Waves Random Media*, vol. 13, pp. 321–337, Oct. 2003.
- [14] F. G. Bass, I. M. Fuks, A. I. Kalmykov, I. E. Ostrovsky, and A. D. Rosenberg, "Very-high frequency radiowave scattering by a disturbed sea surface, Part II: Scattering from an actual sea surface," *IEEE Trans. Antennas Propag.*, vol. AP-16, no. 5, pp. 560–568, Sep. 1968.
- [15] F. Ulaby, R. Moore, and A. K. Fung, *Microwave Remote Sensing: Active and Passive*. Reading, MA: Addison-Wesley, 1982, ch. 12.
- [16] M. A. Tayfun, "On narrow-band representation of ocean waves I. Theory," *J. Geophys. Res.*, vol. 91, no. C6, pp. 7743–7752, Jun. 1986.
- [17] F. Nouguier, C. A. Guerin, and B. Chapron, "Choppy wave model for nonlinear gravity waves," *J. Geophys. Res.*, vol. 114, no. C9, p. C09 012, Sep. 2009.
- [18] D. H. Berman and D. K. Dacol, "Manifestly reciprocal scattering amplitudes for rough interface scattering," *J. Acoust. Soc. Amer.*, vol. 87, no. 5, pp. 2024–2032, May 1990.
- [19] E. Parzen, *Stochastic Processes*. San Francisco, CA: Holden-Day, 1962, pp. 88–97.
- [20] W. J. Plant, E. A. Terray, R. A. Petitt, and W. C. Keller, "The dependence of microwave backscatter from the sea on illuminated area: Correlation times and lengths," *J. Geophys. Res.*, vol. 99, no. C5, pp. 9705–9723, May 1994.
- [21] W. C. Keller, W. J. Plant, R. A. Petitt, and E. A. Terray, "Microwave backscatter from the sea: Modulation of received power and Doppler bandwidth by long waves," *J. Geophys. Res.*, vol. 99, no. C5, pp. 9751–9766, May 1994.
- [22] A. G. Voronovich and V. U. Zavorotny, "Curvature effects in the composite model for low-grazing-angle rough-surface scatter," *Waves Random Media*, vol. 8, no. 1, pp. 41–52, Jan. 1998.
- [23] V. E. Derr, *Remote Sensing of the Troposphere*. Washington, DC: U.S. Govt. Printing Office, 1972, ch. 12.
- [24] B. Chapron, F. Collard, and F. Ardhuin, "Direct measurement of ocean surface velocity from space: Interpretation and validation," *J. Geophys. Res.*, vol. 110, no. C7, p. C07 008, 2005.
- [25] A. D. Rozenberg, D. C. Quigley, and W. K. Melville, "Laboratory study of polarized microwave scattering by surface waves at grazing incidence: Part I—Wind waves," *IEEE Trans. Geosci. Remote Sens.*, vol. 33, no. 4, pp. 1037–1046, Jul. 1995.



Yunhua Wang was born in Shandong, China, in 1978. He received the M.S. and Ph.D. degrees in radio science from Xidian University, Xi'an, China, in 2005 and 2006, respectively.

He is currently with the Ocean Remote Sensing Institute, Ocean University of China, Qingdao, China. His research interests include asymptotic and numerical simulations of electromagnetic wave scattering from random sea surfaces and synthetic aperture radar remote sensing of the ocean.



Yanmin Zhang was born in Shandong, China, in 1979. She received the Ph.D. degree in optics from the Huazhong University of Science and Technology, Wuhan, China, in 2007.

She is currently with the College of Information Science and Engineering, Ocean University of China, Qingdao, China. Her research interests include electromagnetic scattering from sea surfaces and applications for remote sensing.